



NRL/MR/6794--16-9710

Quasi-Static Evolution, Catastrophe, and “Failed” Eruption of Solar Flux Ropes

JAMES CHEN

*Beam Physics Branch
Plasma Physics Division*

December 30, 2016

Approved for public release; distribution is unlimited.

REPORT DOCUMENTATION PAGE				Form Approved OMB No. 0704-0188	
Public reporting burden for this collection of information is estimated to average 1 hour per response, including the time for reviewing instructions, searching existing data sources, gathering and maintaining the data needed, and completing and reviewing this collection of information. Send comments regarding this burden estimate or any other aspect of this collection of information, including suggestions for reducing this burden to Department of Defense, Washington Headquarters Services, Directorate for Information Operations and Reports (0704-0188), 1215 Jefferson Davis Highway, Suite 1204, Arlington, VA 22202-4302. Respondents should be aware that notwithstanding any other provision of law, no person shall be subject to any penalty for failing to comply with a collection of information if it does not display a currently valid OMB control number. <i>PLEASE DO NOT RETURN YOUR FORM TO THE ABOVE ADDRESS.</i>					
1. REPORT DATE (DD-MM-YYYY) 30-12-2016		2. REPORT TYPE Interim		3. DATES COVERED (From - To) March 2016 – June 2016	
4. TITLE AND SUBTITLE Quasi-Static Evolution, Catastrophe, and “Failed” Eruption of Solar Flux Ropes				5a. CONTRACT NUMBER	
				5b. GRANT NUMBER	
				5c. PROGRAM ELEMENT NUMBER	
6. AUTHOR(S) James Chen				5d. PROJECT NUMBER 67-4989-07	
				5e. TASK NUMBER	
				5f. WORK UNIT NUMBER	
7. PERFORMING ORGANIZATION NAME(S) AND ADDRESS(ES) Naval Research Laboratory 4555 Overlook Avenue, SW Washington, DC 20375-5320				8. PERFORMING ORGANIZATION REPORT NUMBER NRL/MR/6794--16-9710	
9. SPONSORING / MONITORING AGENCY NAME(S) AND ADDRESS(ES) Naval Research Laboratory 4555 Overlook Avenue, SW Washington, DC 20375-5320				10. SPONSOR / MONITOR'S ACRONYM(S) NRL	
				11. SPONSOR / MONITOR'S REPORT NUMBER(S)	
12. DISTRIBUTION / AVAILABILITY STATEMENT Approved for public release; distribution is unlimited.					
13. SUPPLEMENTARY NOTES					
14. ABSTRACT This document presents the first theoretical treatment of the dynamical evolution of solar flux ropes subject to slowly increasing magnetic energy, encompassing quasi-static evolution, “catastrophic” transition to an eruptive state, rapid cessation of the eruption, and ensuing quasi-equilibrium evolution. The flux ropes, initialized to be force-free, self-consistently evolve into non-force-free equilibria while maintaining kink stability. In the post-eruption equilibria, tension force of the toroidal self field and the pressure gradient force combine to balance the major radial hoop force. The macroscopic forces on the flux ropes and onset conditions are quantified.					
15. SUBJECT TERMS Solar coronal mass ejections Onset conditions Solar physics theory Failed eruptions Forces					
16. SECURITY CLASSIFICATION OF:			17. LIMITATION OF ABSTRACT Unclassified Unlimited	18. NUMBER OF PAGES 17	19a. NAME OF RESPONSIBLE PERSON James Chen
a. REPORT Unclassified Unlimited	b. ABSTRACT Unclassified Unlimited	c. THIS PAGE Unclassified Unlimited			19b. TELEPHONE NUMBER (include area code) (202) 767-3134

Quasi-Static Evolution, Catastrophe, and “Failed” Eruption of Solar Flux Ropes

James Chen¹

Plasma Physics Division, Naval Research Laboratory, Washington,

DC 20375

This paper presents the first theoretical treatment of the dynamical evolution of solar flux ropes subject to slowly increasing magnetic energy, encompassing quasi-static evolution, “catastrophic” transition to an eruptive state, rapid cessation of the eruption, and ensuing quasi-equilibrium evolution. The flux ropes, initialized to be force-free, self-consistently evolve into non-force-free equilibria while maintaining kink stability. In the post-eruption equilibria, tension force of the toroidal self field and the pressure gradient force combine to balance the major radial hoop force. The macroscopic forces on the flux ropes and onset conditions are quantified.

Solar eruptions—coronal mass ejections (CMEs), flares, and prominence eruptions—have been conceptualized as processes consisting of quasi-static build-up and ensuing rapid release of stored magnetic energy, usually attributed to “some” catastrophic loss of equilibrium or instability. This possible catastrophic transition to an eruptive state has been studied using idealized two-dimensional (2-D) structures such as linear arcades^{1–3} and flux ropes^{4–7}. The kink instability is most often invoked as the cause of the onset of eruptions. The early calculations used infinitely long straight flux ropes as an idealized model of large-aspect ratio flux ropes^{8,9}, but extensions to straight flux ropes of finite length with line-tied ends have been made^{10,11}.

Recent observations and theoretical calculations have shown that CMEs and eruptive prominences are consistent with being expanding toroidal magnetic flux ropes based on both morphological *and* dynamical properties^{12–14}, and observed CMEs are now interpreted as such^{15,16}. The physical processes involved in the onset of flux-rope eruption have attracted renewed interest^{17–19}. Kliem and Török¹⁸ proposed the so-called “torus instability” (TI) as the mechanism that leads to the onset and acceleration of flux-rope CMEs. This condition has been widely used to interpret observations with some ambiguous results^{19,20}.

Laboratory experiments were recently conducted to simulate the expansion of partial toroidal pinches with stationary footpoints that may be scalable to solar flux ropes^{21,22}. The former studied the expansion of quasi-stationary flux ropes through a background plasma in response to injection of plasma and poloidal flux²¹, and the latter showed that the flux ropes can exhibit the so-called “failed” or “confined” eruption²². In such events on the Sun, prominence eruptions stop after reaching, say, 200–300 km s^{−1}, becoming quasi-stationary at new heights^{23,24}. In Myers et al.’s work²², the cessation of the eruption was attributed to a transient surge in the tension force of the toroidal (guide) field. They compared their results to the TI model and noted that the model lacks a toroidal magnetic field and its tension so that it cannot model failed eruptions on the Sun or in the experiment. By extension, this also raises issues regarding the TI onset condition based on unbalancing forces. More broadly, they identified this as an essential deficiency in the current theoretical CME models. Indeed, there is as yet no theory to self-consistently model slow pre-eruption evolution leading to eruption of CME-like flux ropes under quasi-static build-up of coronal magnetic energy, the long-standing paradigm of solar eruptions.

This paper presents the first theoretical model—a single consistent set of flux-rope equa-

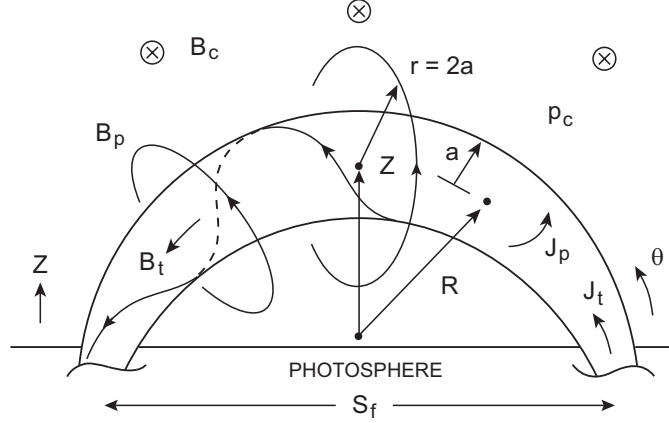


FIG. 1. Solar flux rope. The footpoints are stationary ($S_f = \text{const}$). The current channel of major radius R and minor radius a has toroidal (I_t) and poloidal (I_p) currents, producing self-field components, B_p and B_t , respectively. θ is measured from the footpoint and Z from Sun center.

tions of motion—to describe as one continuous dynamical process the quasi-static flux rope evolution, catastrophic loss of equilibrium and onset of eruption, cessation of eruption, and the post-eruption quasi-equilibria. The solutions show that the three-dimensional (3-D) flux rope is stable to kink. Motivated by Ref.²², the forces and their evolution throughout the process are quantified.

Figure 1 shows a schematic of the model configuration with the following features. It is a toroidal flux rope embedded in the corona, with the two footpoints separated by $S_f = \text{const}$. Here, “toroidal” refers to a section of a torus. The flux rope is defined by a current loop (major radius R and minor radius a) and its magnetic field. The centroid of the apex is at height Z (from Sun center). Major radius $R(\theta)$ is taken to be uniform along the flux rope, but $a(\theta)$ varies with θ : at the apex, $a(\theta = \pi) = a_a$, and at the footpoints, $a(\theta_f) = a_f$. If unsubscripted, $a = a_a$ is understood.

The current channel carries toroidal and poloidal currents, I_t and I_p , producing B_p and B_t , respectively, via Ampere’s law. The current is localized within the channel, *i.e.*, $\mathbf{J}(r \geq a) = 0$, where r is the minor radial coordinate. Thus, $I_t \equiv 2\pi \int_0^a J_t(r) r dr$ and $I_p \equiv 2\pi R \int_0^a J_p(r) dr$, with $B_{pa} \equiv B_p(r = a) = 2I_t/ca$. Outside the current channel ($r > a$), $B_p(r) \sim B_{pa}a/r$. By fiat, the flux rope is taken to be limited to $r \leq 2a$, beyond which $B_p(r) \sim B_{pa}/2$ may be too weak to be distinguished from the ambient field. Representative magnetic field “lines” are drawn. The toroidal flux is $\Phi_t = 2\pi \int_0^a B_t(r) r dr \equiv \pi \bar{B}_t a^2$, and $\Phi_t = \text{const}$ is assumed,

where \bar{B}_t is the minor radial average.

The flux rope has average internal pressure \bar{p} , embedded in the corona of pressure $p_c(Z)$ and magnetic field $B_c(Z)$. Here, B_c is perpendicular to the plane of the flux rope. These system parameters have been defined elsewhere²⁵. There can be an external toroidal component B_{ct} , which will not be treated because of space limitation and the need to introduce a spatial model $B_{ct}(Z)$.

The ideal MHD force density is given by $\mathbf{f} = (1/c)\mathbf{J} \times \mathbf{B} - \nabla p + \rho \nabla \phi_g$, ρ is mass density, and ϕ_g is the gravitational potential. The volume-integrated major radial force per unit length at the apex is given by^{25,26}

$$M \frac{d^2 Z}{dt^2} = \frac{\Phi_p^2(t)}{c^4 L^2 R} f_R(t) + F_d + F_g, \quad (1)$$

where $M \equiv \pi a^2 \bar{\rho}$ is the mass per unit length, and

$$f_R(t) \equiv \ln \left(\frac{8R}{a} \right) + \frac{\beta_p}{2} - \frac{\bar{B}_t^2}{2B_{pa}^2} + \frac{2R}{a} \frac{B_c}{B_{pa}} - 1 + \frac{\xi_i}{2}. \quad (2)$$

Here, $\beta_p \equiv 8\pi(\bar{p} - p_c)/B_{pa}^2$ is pressure gradient $(\partial p/\partial r)$ integrated over a . The minor radius $a(t)$ is governed by

$$M \frac{d^2 a}{dt^2} = \frac{I_t^2}{c^2 a} \left(\frac{\bar{B}_t^2}{B_{pa}^2} - 1 + \beta_p \right). \quad (3)$$

In equation (1), $\Phi_p(t) \equiv cL(t)I_t(t)$ is the poloidal flux of the flux rope, so that $\Phi_p^2/c^4 L^2 = I_t^2/c^2$. Neglecting F_d and F_g for now, the equation can be written as

$$\frac{d^2 Z}{dt^2} = \frac{R}{\tau_R^2} f_R, \quad (4)$$

where $\tau_R \equiv R/V_{Ap}$ with $V_{Ap} \equiv B_{pa}/(4\pi\bar{\rho})^{1/2}$. Thus, the acceleration timescale is the Alfvén transit time τ_R . For the main acceleration phase, τ_R depends on the initial equilibrium values of $\bar{\rho}_0$ and B_{pa0} .

The toroidal geometry enters the equations via the constraint

$$R(t) = \frac{\tilde{Z}^2(t) + S_f^2/4}{2\tilde{Z}(t)}, \quad (5)$$

where $\tilde{Z} \equiv (Z - R_\odot)$. That is, at any time, $R(t)$ is determined by $S_f = \text{const}$ and apex height above the photosphere $\tilde{Z}(t)$. The self-inductance $L(t)$ relates the current I_t to the poloidal energy $U_p = (1/2)LI_t^2$ and is given by²⁷

$$L(t) = \frac{4\pi\Theta R}{c^2} \left\{ \frac{1}{2} \left[\ln \left(\frac{8R}{a_f} \right) + \ln \left(\frac{8R}{a_a} \right) \right] - 2 + \frac{\xi_i}{2} + \Delta \right\} \quad (6)$$

where $2\pi\Theta(t)R(t)$ is the length of the evolving flux rope and $\Theta(t)$ is the fraction of a complete circle. The additive quantity $\Delta(t)$ is a geometrical factor and is determined by how $a(\theta)$ increases from a_f to a_a , with $\Delta(t) = 0$ for $a(\theta) = \text{const}$ or $a(\theta) \sim \exp[(\theta - \theta_f)/s]$, where $s = \text{const}$. We will use exponential dependence so that $\Delta(t) = 0$. For CME-like flux ropes with linear $a(\theta)$, $|\Delta| \simeq 0.1\text{--}0.3$.

The drag force per unit length is modeled by

$$F_d = 4c_d\rho_c a\Delta V|\Delta V|, \quad (7)$$

where $\Delta V \equiv V_c - (V + 2w)$, $V \equiv dZ/dt$ is the speed of the centroid of the apex at $Z(t)$, $w(t) \equiv da(t)/dt$, and c_d is the drag coefficient. The term $(V + 2w)$ is the speed of the outermost magnetic surface of the flux rope ($r = 2a$) and arises from the definition of the leading edge (LE), $Z_{LE} = Z + 2a$ (Figure 1), so that $V_{LE} = d(Z + 2a)/dt = V + 2w$. The values of c_d suitable for coronal and solar wind applications have been found to be in the range of 0.1–3 in an MHD simulation study²⁸, and $c_d = 1$ is used in the calculations here.

The terms in f_R were originally derived by Shafranov²⁹ for axisymmetric tokamak equilibria in vacuum. Equations (1) and (3) were applied to the dynamics of non-axisymmetric solar flux ropes with $S_f = \text{const}$ and constraint (5), including drag coupling to the ambient corona²⁶. The hoop force for arbitrary $a/R \ll 1$ was later rigorously derived³⁰. The hoop force is now familiar in the solar context^{18,22,25,28,31}.

The initial coronal loop is defined by footpoint separation S_f , apex height Z_0 , and aspect ratio R_0/a_0 , with average internal pressure \bar{p}_0 . Major radius R_0 is calculated from S_f and Z_0 . The structure is in equilibrium with coronal pressure $p_{c0} \equiv p_c(Z_0)$ and overlying magnetic field $B_{c0} \equiv B_c(Z_0)$. Given the initial geometry and coronal parameters p_{c0} and B_{c0} , the equilibrium force balance conditions, $d^2Z/dt^2 = 0$ and $d^2a/dt^2 = 0$, are imposed. These conditions determine the initial equilibrium field $B_{pa0} \equiv B_p(r = a|t = 0)$

$$B_{pa0} = 2 \left(\frac{R_0}{a_0} \right) [\Lambda_0 + \beta_{p0} - 4\pi m_i R_0 g_0 (\bar{n}_0 - n_{c0})] |B_{c0}|, \quad (8)$$

so that $B_{pa0} \propto (R_0/a_0)|B_{c0}| > |B_{c0}|$. Here, $\Lambda_0 \equiv \ln(8R_0/a_0) - (3/2) + (\xi_i/2)$. Equation (3) yields the toroidal field $\bar{B}_{t0}^2 = (1 - \beta_{p0})B_{pa0}^2$. Thus, B_p and \bar{B}_t both critically depend on the toroidal geometry (R/a). With $B_c \neq 0$, it is possible to choose a force-free initial equilibrium. Thus, we will use $\beta_{p0} = 0$ in which case $\bar{B}_{t0} = B_{pa0}$. The structure, however, is not assumed to evolve force-free, i.e., $\beta_p(t) \neq 0$ for $t > 0$.

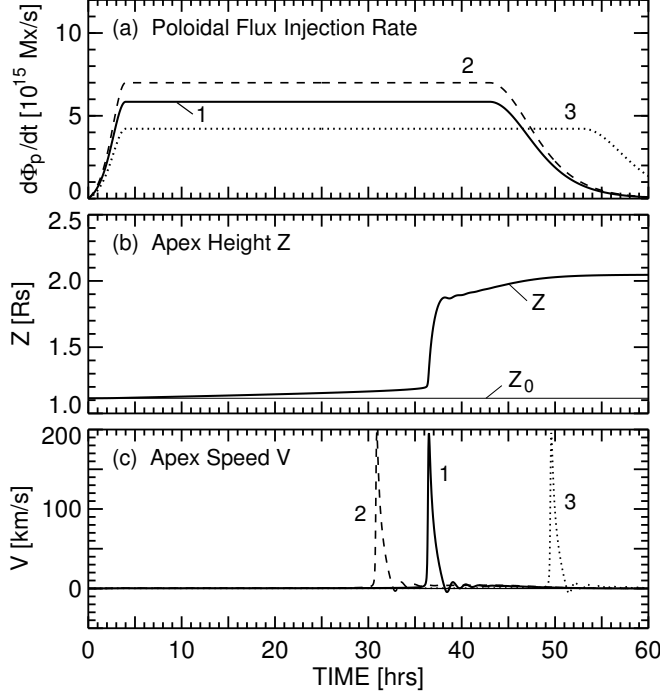


FIG. 2. Quasi-static evolution. (a) Profiles of $d\Phi_p(t)/dt$. The reference profile (solid curve) is labeled “1.” Respectively, profiles “1,” “2,” and “3” have $(d\Phi_p/dt)_{max} = (5.8, 7.0, 4.2) \times 10^{15}$ Mx s $^{-1}$. (b) Height of the apex $Z(t)$ $Z_0 = 1.11R_\odot$ is indicated. (c) Speed of the apex, $V = dZ/dt$. Solutions “1,” “2,” and “3” for the three $d\Phi_p(t)/dt$ profiles in panel (a).

The discussion below will treat a CME-like flux rope to illustrate the theory in real units so that the theoretical results may be directly related to observations. The initial flux rope is specified by $S_f = 1 \times 10^5$ km, $Z_0 = 8.0 \times 10^4$ km, and $R_0/a_0 = 2$ ($a_0 = 2.8 \times 10^4$ km), giving $R_0 = 5.6 \times 10^4$ km. The coronal parameters at $Z = Z_0$ are $B_{c0} = -4.0$ G and $p_{c0} = 0.32$ dyn cm $^{-2}$. With $\bar{T}_0 = T_{c0} = 2 \times 10^6$ K, we have $\bar{n}(0) = 5.8 \times 10^8$ cm $^{-3}$. These values yield $B_{pa}(0) = \bar{B}_{t0} = 8.64$ G, so that $\tau_R = R_0/V_{Ap0} = 72$ sec with $V_{Ap0} = 783$ km s $^{-1}$. The total mass of this flux rope is $M_T = 1.1 \times 10^{15}$ g. The initial poloidal flux is $\Phi_p(0) = 7.4 \times 10^{20}$ Mx (cgs) and $\Phi_t = 2.1 \times 10^{20}$ Mx.

We now slowly increase Φ_p , i.e., the magnetic field “twist,” by specifying $d\Phi_p(t)/dt$ as shown in Figure 2a. The maximum rate is $(d\Phi_p/dt)_{max} = 5.8 \times 10^{15}$ Mx s $^{-1}$, which is sustained for approximately 40 hours, with $\Phi_p(t = 60) \approx 2.3\Phi_{p0}$. This is designated as the reference profile (solid curve “1”). The injection rate is “slow” on the acceleration timescale τ_R , satisfying $(d\Phi_p/dt)_{max} \ll (\Phi_{p0}/\tau_R) \approx 10^{19}$ Mx s $^{-1}$. As $\Phi_p(t)$ increases, the terms in f_R

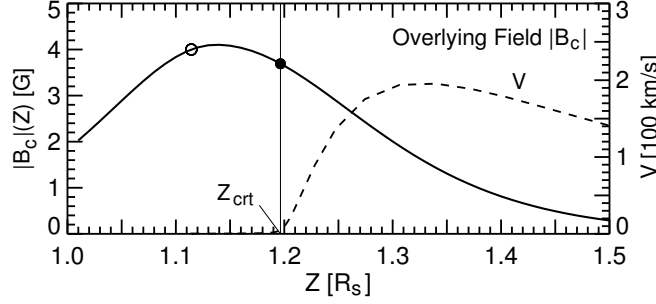


FIG. 3. Potential barrier due to $B_c(Z)$ (solid) and critical height $Z_{crit} = 1.18R_\odot$ of loss of equilibrium. Apex velocity $V(Z)$ (dashed).

become unbalanced ($f_R > 0$), and the flux rope rises. Panels 2b and 2c show the evolution of the flux rope. The solution shows that the apex of the flux rope Z slowly rises until about $t = 36$ hrs when it starts to erupt. This eruption, however, “fails” to sustain itself after reaching the peak speed of $V \approx 200 \text{ km s}^{-1}$. The apex velocity $V(t)$ for this solution is shown in panel c (curve “1”). The value of Φ_p remains virtually unchanged during the eruption. Post-eruption, the flux rope reverts to quasi-equilibrium evolution at greater heights and tends to a new equilibrium as $d\Phi_p/dt \rightarrow 0$. The full-width-at-half-maximum (FWHM) duration of the velocity peak is $\Delta t \approx 30 \text{ min}$.

Another solution was obtained for the same initial flux rope subject to a faster rate of flux injection (“2”, panel a): $(d\Phi_p/dt)_{max} = 7.0 \times 10^{15} \text{ Mx s}^{-1}$. The pre-eruption rise is slightly faster, reaching the same critical point earlier. The apex speed is shown in Figure 2c (dashed, “2”). Except for the shift in time, the profile of $V(t)$ is indistinguishable from that of solution 1. The eruption is insensitive to the value of $d\Phi_p/dt$ provided $(d\Phi_p/dt)_{max} \ll \Phi_{p0}/\tau_R$. This is because τ_R does not depend on $d\Phi_p/dt$. Profile “3” (dotted) has a slower rate $(d\Phi_p/dt)_{max} = 4.2 \times 10^{15} \text{ Mx s}^{-1}$. The apex velocity profile, labeled “3” (dotted) in Figure 2c is again unchanged except that Z_{crit} is reached later. The same profile of failed eruption is obtained as the rate $(d\Phi_p/dt)_{max}$ is made smaller (not shown).

Figure 3 shows the magnitude of the external magnetic field $|B_c(Z)|$ (solid curve), which produces a downward force ($I_t B_c$) so that the peak in $|B_c(Z)|$ represents an effective potential barrier. The initial apex position of the flux rope, $Z_0 \approx 1.11R_\odot$, is indicated by the open circle. This shows that the flux rope, which is stable to major radial expansion, must overcome the barrier. As Φ_p increases slowly, the flux rope rises (Figure 2b). The solid circle indicates Z_{crit} , height of the “onset” of the eruption, which is arbitrarily chosen to be

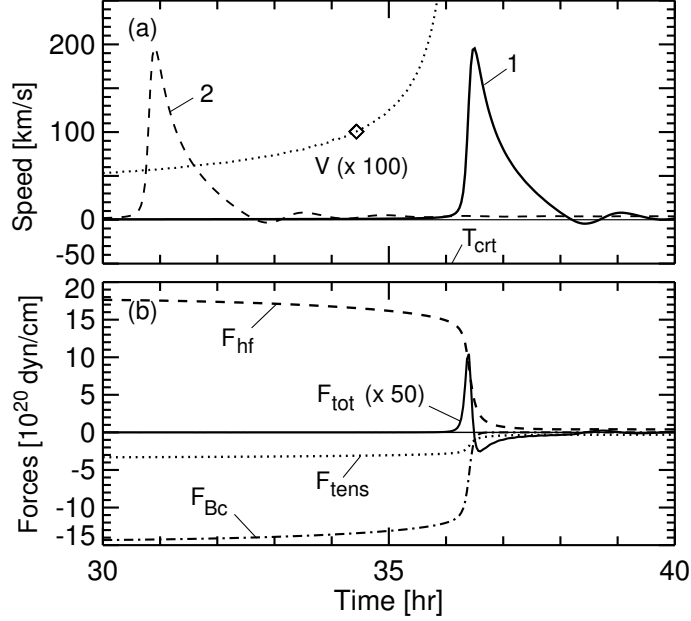


FIG. 4. Dynamics during the failed eruption. (a) $V(t)$ for solutions “1” (solid) and “2” (dashed). Curve “1” magnified by 100 (dotted). Diamond: $V = 1 \text{ km s}^{-1}$. (2) Forces. F_{hf} : hoop force. F_{Bc} : $I_t B_c$. F_{tens} : tension, the \bar{B}_t^2/B_{pa}^2 term in equation (2). The net force F_{tot} is magnified by 50.

when $V = 5 \text{ km s}^{-1}$ is reached. For solution 1, $Z_{crt} = 1.20 R_\odot$, which occurs at $T_{crt} = 36.1 \text{ hr}$. To show the relationship of V to $B_c(Z)$, the apex velocity is shown as a function of Z (dashed, right vertical axis). The onset height Z_{crt} , well past the peak of $|B_c|$, is the same for all three solutions shown in Figure 2c.

The apex velocity $V(t)$ and the forces on the flux rope are shown on an expanded timescale in Figure 4. The curves marked “1” (solid) and “2” (dashed) are the respective curves in Figure 2c. T_{crt} for solution 1 is marked. Figure 4a also shows velocity curve “1” multiplied by 100 (dotted). The open diamond designates the time before which $V < 1 \text{ km s}^{-1}$. This is much earlier than $t = T_{crt}$. Figure 4b shows the various force terms in equation (1): the hoop force F_{hf} arises from $J_t B_p$, tension $F_{tens} \propto -B_t^2/B_{pa}^2$ from the self field B_t , $F_{Bc}(< 0)$ from $I_t B_c$ term, and $F_p \propto \beta_p$ from $dp/dr \neq 0$. The net major radial force is denoted by F_{tot} . The initial equilibrium ($F_{tot} = 0$) is established by $F_{hf} = -(F_{Bc} + F_{tens})$, with F_{tens} playing a relatively minor role. Because $\beta_{p0} = 0$ is chosen, $F_{p0} = 0$ at $t = 0$. Except during the eruption, F_d is negligible because $\Delta V \approx 0$ in equation (7). Gravity is negligible.

Figure 5 shows forces on an expanded vertical scale. The net force F_{tot} driving the failed eruption is a relatively small imbalance between F_{Bc} and F_{hf} (Figure 4b), but the post-

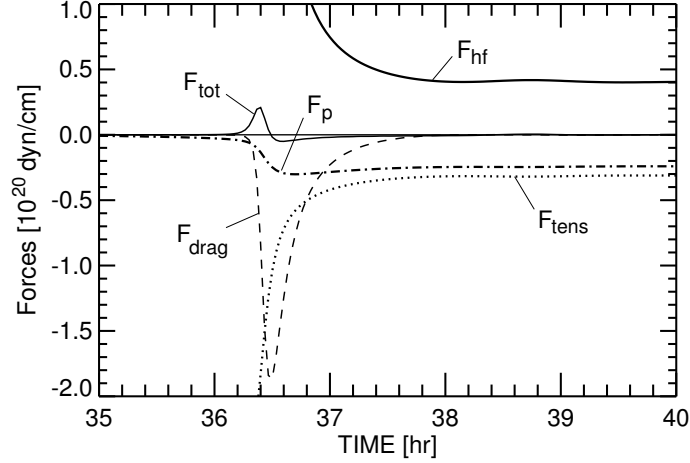


FIG. 5. Evolution of forces. All forces are shown in real units. F_{tot} includes all terms in equation (1), coupled to equation (3). $|F_p|$ increases during the eruption, establishing a new non-force-free equilibrium, $F_p \neq 0$. F_{Bc} rapidly vanishes before $t = 36.6$ and, for clarity, is not shown.

eruption equilibria are established by $F_{hf} = -(F_p + F_{tens})$ with comparable F_p and F_{tens} and $F_{Bc} \approx 0$. (For clarity, F_{Bc} is not shown; it becomes negligible— $|F_{Bc}| \ll |F_{tens} + F_p|$ —by $t \approx 36.6$ hrs.) Although the initial flux rope is force-free ($F_{\mathbf{J} \times \mathbf{B}} = F_p = 0$), it becomes strongly non-force-free ($F_p \sim F_{tens}$). Thus, it is essential to include the β_p term in the equation of motion. Note that $F_{p0} = 0$ at $t = 0$ is possible because $B_c \neq 0$. If $B_c = 0$, then $F_p \neq 0$ is necessary for equilibrium³².

The expansion prior to and after the failed eruption is quasi-static: it can be made arbitrarily slow by taking the limit $(d\Phi_p/dt)_{max} \rightarrow 0$ and increasing the duration of flux injection. The three solutions in Figure 2c illustrates this limiting process. Given $B_c(Z)$ and $p_c(Z)$, the velocity and timescale τ_R are independent of how the limit is taken (Figure 4a), being determined by the intrinsic flux rope properties such as the geometry and self magnetic field. The transition to eruption is *catastrophic* in that τ_R is finite.

Numerical simulations of the evolution of arcades under “slow” driving of footpoints have been carried out^{33–35}. In such studies, the lower boundaries are placed at the base of the corona, and for numerical tractability, the footpoints are driven much faster than the photospheric speeds of observed magnetic features (e.g., up to tens of kilometers per second in the above simulations). To the extent that large coronal structures and photospheric magnetogram features (e.g., active regions) nearly co-rotate, such high speeds on the scale of eruptive arcades would require comparably fast speeds the photosphere. These simulations

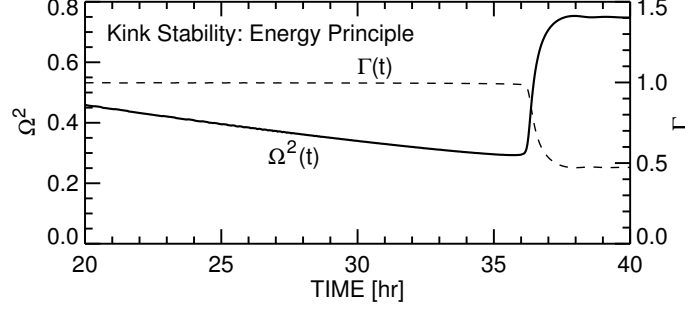


FIG. 6. Instantaneous value of $\Omega^2(t) \equiv \omega^2/V_{Ap}^2 k^2$ (solid curve). Kadomtsev condition for kink stability.: $\Omega^2 > 0$ means stable oscillatory motion. Characteristic magnetic pitch $\Gamma(t) \equiv B_{pa}(t)/\bar{B}_t(t)$ (dashed curve). The values are shown on the right vertical axis.

show coronal response on the Alfvén transit time similar to τ_R . In these simulations, the onset of eruption depends on various “tether cutting” processes via reconnection, which dynamically reduces the effective potential barrier.

To examine the kink stability of the flux rope with no guide field, we apply the Kadomtsev condition based on an energy principle, which yields the eigenfrequency³⁶

$$\omega^2 = V_{Ap}^2 k^2 \left[1 - \Gamma^2(t) \ln \left(\frac{1}{ka} \right) \right], \quad (9)$$

where is $\Gamma(t) \equiv B_{pa}(t)/\bar{B}_t(t)$ is the characteristic magnetic pitch and k the toroidal wavenumber. The flux rope is stable if $\omega^2 > 0$. For the longest wavelength between the stationary footpoints, we have $1/ka = \Theta R/a$. Figure 6 shows $\Omega^2(t) \equiv \omega^2/V_{Ap}^2 k^2 > 0$ (solid). This shows that the flux rope is stable to the kink ($\Omega^2 > 0$) at $t = 0$ and throughout the quasi-equilibrium expansion. The flux rope evolves to a more stable configuration (more positive Ω^2) during the failed eruption. There is no external toroidal guide field ($B_{ct} = 0$).

Also plotted in Figure 6 is magnetic pitch $\Gamma(t)$ (dashed); it decreases during the eruption but is otherwise virtually constant. This is equivalent to tension, $\bar{B}_t(t)/B_p(t) = \Gamma^{-1}(t) \sim \Theta R/a$, increasing relative to the hoop force. Both render the flux rope even more kink stable. These two effects are coupled, due to a number of dynamical effects: $R(t)$ and therefore $L(t)$ increase so that $I_t(t) \propto 1/L \sim 1/R(t)$ decreases; $a(t)$ expands rapidly, causing $B_p \propto I_t/a$ and $\bar{B}_t(t) \propto \Phi_t/a^2(t)$ to decrease; F_{hf} does work against F_{tens} during the expansion, equation (1), so that B_t gains energy from B_p . The expansion in $a(t)$ causes $\bar{p}(t)$ to decrease independently of $p_c(Z)$, and $F_p \propto \beta_p$ becomes nonzero (non-force-free). These dynamical quantities evolve self-consistently according to equations (1) and (3), which determine the inductance $L(t)$

and therefore the evolution of the magnetic field. This is a fully 3-D ideal MHD process.

The above discussion shows that the minor radial dynamics $a(t)$ are fundamental to the evolution of major radial forces. Figure 7 gives the dynamics of $a(t)$ and $R(t)/a(t)$, where $a(t)$ and $R(r)$ are determined by coupled equations (1)–(6). It shows that $a(t)$ (solid) rapidly expands during the failed eruption while $R(t)/a(t)$ (dashed) undergoes a slight decrease when $V(t)$ peaks: $a(t)$ expands faster than $R(t)$ during this time. Past this point, $a(t)$ and $R(t)/a(t)$ both increase, showing that major radial expansion dominates again. Throughout the process, $R(t)/a(t) \neq \text{const}$. This is in contrast to the assumption of $R(t)/a(t) = \text{const}$ in the TI model¹⁸, which is not made in the calculations of Ref.³¹. The nontrivial variation in $R(t)/a(t)$ shows that it is essential to solve the coupled equations (1) and (3).

The eruption described above is consistent with failed eruptions on the Sun^{23,24}. The velocity profile in Figure 4a resembles the observed profile reported in Figure 2e of Ref.²⁴, including a damped oscillation. The FWHM duration Δt of the velocity peak is several minutes²³ to a few tens of minutes²⁴. The failed eruption was interpreted as “probably due to the strong strapping field.” The strength of this field is not measured but should be weaker at the new height. For the model flux rope, the strapping field B_c vanishes, and it is \bar{B}_t and dp/dr that provide the equilibrium.

For the flux ropes in the experiment²², Myers et al. analyzed the forces in terms of integrated quantities as in equations (1) and (3). In one regime, the flux ropes stabilized against the kink by a sufficiently strong toroidal guide field exhibited failed eruption, returning to nearly the original height after the eruption. They observed a transient surge in the toroidal guide field and its tension force during the eruption, which was identified as the cause of the failed eruption. Based on their analysis and the lack of toroidal fields in the TI equation, Myers et al. concluded that the TI model—by extension other models with no toroidal fields—cannot explain the laboratory or observed failed eruptions, or the onset condition. The TI equation is a special case of equation (1) with $\beta_p = 0$ and $B_t = 0$. In this limit, both F_{tens} and F_p are absent, the two forces that determine the failed eruption and subsequent equilibria. This is also reflected in the fact TI solutions do not exhibit any oscillations that are often observed²⁴. The forces and the length $S_f = \text{const}$ in the experiment better correspond to those in equations (1)–(5) than the TI equation.

It is noted that no external guide field (B_{ct}) or strapping field (B_c) is required to confine the eruption: the forces involved in the failed eruption and the subsequent non-force-free

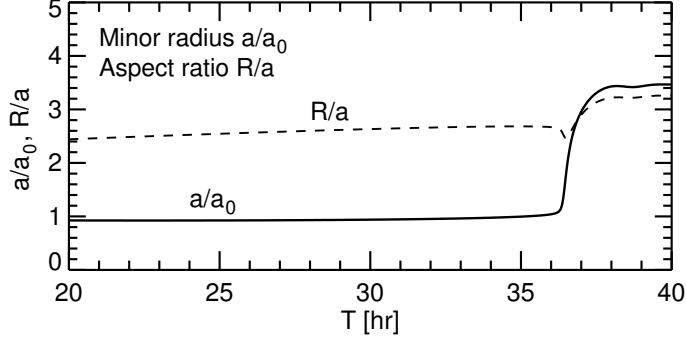


FIG. 7. Dynamics of minor radius $a(t)/a_0$ and aspect ratio $R(t)/a(t)$.

equilibrium discussed herein are due to self fields and pressure gradient.

The results of the present work are consistent with the argument of Myers et al. that toroidal tension force is the cause of failed eruptions²². There are, however, significant differences. The model system has no conducting vessel nor an external magnetic field. The self B_t and its tension exhibit no surge during the eruption, and the equilibrium flux rope organized by self fields and ambient pressure is kink stable. Indeed, pressure force, $F_p \propto \beta_p$ —not considered in TI and interpretations of observations and the experiment results—is comparable to F_{tens} . In the experiment, a conversion of Φ_p to Φ_t was inferred. This implies the presence of non-ideal or inductive effects. In the theory, there is no flux conversion because $\Phi_t = const$, but B_p does work on B_t . The surge detected in the experiment is attributed to the interaction between the expanding flux rope and the applied guide field. This interaction may involve the conducting wall (e.g., image currents) and external circuit. Assessment of such laboratory factors is identified as an open question for further work.

There is an ambient medium ($p_c \neq 0$) so that $\beta_p < 0$ in the post-eruption equilibria. The dynamics shown in Figure 4 are critically determined by the self fields $B_t(t)$, $B_p(t)$, and pressure gradient $dp(t)/dr$, with the drag force being significant only during the eruption. The model flux rope reaches a new equilibrium height while the flux ropes in the experiment return to the initial positions. In observed failed eruptions, prominences typically do not return to the initial heights.

The TI model defines the onset condition for an axisymmetric torus with no footpoints using the so-called decay index $n \equiv -[(Z/B_c)dB_c/dZ]_{crt}$. In the experiment, the failed eruptions occupy the n - q parameter space region, $0.8 < n < 4$ (TI unstable) and $0.8 < q < 1.8$ (kink stable), where $q \equiv (a/\Theta R)\bar{B}_t/B_{pa}$ is the safety factor. Because of the different form

of $B_c(Z)$ and force terms in the TI equation, there are no directly comparable quantities here. Nevertheless, *formally*, the above quantities are $q \approx 0.5$ and $n \approx 2$ for the present flux rope. Here, the characteristic value of q is based on \bar{B}_t because there is no external guide field. The TI prediction is $n_{cr} \approx 0.8$. The difference arises from the toroidal magnetic tension force F_{tens} due to the self field B_t . The onset condition given by the more general treatment^{31,37}, having $F_p \neq 0$, $F_{tens} \neq 0$, and $S_f = const$, are applicable to the model and solar flux ropes.

An observed failed filament eruption²³ was simulated using an MHD model³⁸. The initial structure is a kink-unstable flux rope with fixed footpoints. There is an applied toroidal field specified by a fictitious subphotospheric line current. The structure is assumed to be force-free. The simulation, with increased diffusion to prevent numerical instabilities, shows that the kink instability grows and then saturates, which is attributed to (numerical) reconnection above the flux rope. No evolution to the unstable initial state is given. The failed eruption here is non-force-free and kink stable, and requires no reconnection. Nevertheless, the major radial forces (without the external field) should be describable by equations (1) and (3).

There are several straight 2-D models of catastrophic transition⁵⁻⁷. They typically use force-free ($F_p = 0$) cylindrical flux ropes with no internal toroidal field, in which the upward force arises from the repulsion from photospheric image currents. In 3-D flux ropes, the force from the photospheric return current is insignificant relative to the hoop force unless $Z/S_f \ll 1$ ³⁰. There is no 2-D counterpart of the major radial forces.

The paper has presented the first theoretical calculation of quasi-static evolution, catastrophic loss of equilibrium, failed eruption, and re-establishment of new toroidal equilibrium. The driver of the evolution is a quasi-static increase in the poloidal magnetic energy ($\propto \Phi_p^2$). Physically, this may arise from slow differential twist in the footpoints or changes in the current below the photosphere. The key findings are: (1) an initial force-free flux rope evolves into a non-force-free flux rope maintaining kink stability and (2) the onset of eruption, cessation of the eruption, and the post-eruption equilibria are critically determined by the toroidal self field and pressure gradient, i.e., by $F_{hf} - (F_{tens} + F_p)$, which have been neglected in previous theoretical models. The rapid decrease in F_{hf} is governed by $L(t) \propto R(t) \ln(R/a_f)$. The model dynamics are idealized but are fully 3-D, with equations (1)–(8) coupling the features in Figure 1.

The work was supported by the Naval Research Laboratory Base Research Program.

REFERENCES

- ¹Low, B. C., *Astrophys. J.*, **212**, 234 (1977).
- ²Jockers, K., *Solar. Phys.*, **56**, 37 (1978).
- ³Finn, J. M., and Chen, J., *Astrophys. J.*, **349**, 345 (1990).
- ⁴van Tend, W., and Kuperus, M., *Solar Phys.*, **59**, 115 (1978).
- ⁵Forbes, T. G., *J. Geophys. Res.*, **95**, 11919 (1990).
- ⁶Forbes, T. G., and Isenberg, P. A., *Astrophys. J.*, **373**, 294 (1991).
- ⁷Isenberg, P. A., Forbes, T. G., and Démoulin, P., *Astrophys. J.*, **417**, 368 (1993).
- ⁸Sakurai, T., *Publ. Astron. Soc. Jpn*, **28**, 177 (1976).
- ⁹Hood, A. W., and Priest, E. R., *Solar Phys.*, **64**, 303 (1979).
- ¹⁰Velli, M., Einaudi, G., and Hood, A. W., *Astrophys. J.*, **350**, 428 (1990).
- ¹¹Ryutov, D. D., Cohen, R. H., and Pearlstein, L. D., *Phys. Plasmas*, **11**, 4740 (2004).
- ¹²Chen, J., Howard, R. A., Brueckner, G. E., Santoro, R., Krall, J., Paswaters, S. E., St. Cyr, O. C., Schwenn, R., Lamy, P., and Simnett, G. M., *Astrophys. J. Lett.*, **490**, L191, (1997).
- ¹³Wood, B. E., Karovska, M., Chen, J., Brueckner, G. E., Cook, J. W., and Howard, R. A., *Astrophys. J.*, **512**, 484 (1999).
- ¹⁴Krall, J., Chen, J., Duffin, R. T., Howard, R. A., and Thompson, B. J., *Astrophys. J.*, **562**, 1045 (2001).
- ¹⁵Thernisien, A. F. R., Howard, R. A., and Vourlidas, A., *Astrophys. J.*, **652**, 763 (2006).
- ¹⁶Krall, J., *Astrophys. J.*, **657**, 559 (2007).
- ¹⁷Török, T., Kliem, B., and Titov, V. S., *Astron. Astrophys.*, **413**, L27 (2004).
- ¹⁸Kliem, B., and Török, T., *Phys. Rev. Lett.*, **96**, 255002 (2006).
- ¹⁹Démoulin, P., Vourlidas, A., Pick, M., and Bouteille, A., *Astrophys. J.*, **750**, 147 (2012).
Erratum: *Astrophys. J.*, **754**, 156 (2012).
- ²⁰Liu, Y., *Astrophys. J. Lett.*, **679**, L151 (2008).
- ²¹Tripathi, S. K. P., and Gekelman, W., *Sol. Phys.*, **286**, 479 (2013).
- ²²Myers, C. E., Yamada, M., Ji, H., Yoo, J., Fox, W., Jara-Almonte, J., Savcheva, A., and DeLuca, E. E., *Nature*, **528**, 526 (2015).
- ²³Ji, H., Wang, H., Schmahl, E. J., Moon, Y.-J., and Jiang, Y., *Astrophys. J.*, **595**, L135 (2003).

- ²⁴Cheng, X., Hao, Q., Ding, M. D., Liu, K., Chen, P. F., Fang, C., and Liu, Y. D., *Astrophys. J.*, **809**, 46 (2015).
- ²⁵Chen, J., *J. Geophys. Res.*, **101**, 27499 (1996).
- ²⁶Chen, J., *Astrophys. J.*, **338**, 453 (1989).
- ²⁷Chen, J., and Garren, D. A., *Geophys. Res. Lett.*, **20**, 2319 (1993).
- ²⁸Cargill, P. J., Chen, J., Spicer, D. S., and Zalesak, S. T., **101**, 4855 (1996).
- ²⁹Shafranov, V. D., *Reviews of Plasma Physics*, Vol. 2, ed. M. A. Leontovich, p. 103, Consultants Bureau, New York (1966).
- ³⁰Garren, D. A., and Chen, J., *Phys. Plasmas*, **1**, 3425 (1994).
- ³¹Olmedo, O., and Zhang, J., *Astrophys. J.*, **718**, 433 (2010).
- ³²Xue, M. L., and Chen, J., *Solar Phys.*, **84**, 119 (1983).
- ³³Linker, J. A., Mikić, Z., Lionello, R., Riley, P., Amari, T., and Odstrcil, D., *Phys. Plasmas*, **10**, 1971 (2003).
- ³⁴Lynch, B. J., Antiochos, S. K., Li, Luhman, Y., J. G., and DeVore, C. R., *Astrophys. J.*, **697**, 1918 (2009).
- ³⁵Karpen, J. T., Antiochos, S. K., and DeVore, C. R., *Astrophys. J.*, **760**, 81 (2012).
- ³⁶Kadomtsev, B. B., in *Reviews of Plasma Physics*, **2**, Consultants Bureau, New York, p. 178 (1966).
- ³⁷Cargill, P. J., Chen, J., and Garren, D. A., *Astrophys. J.*, **423**, 854 (1994).
- ³⁸Török, T., and Kliem, B., *Astrophys. J.*, **630**, L97 (2005)

